Agricultural and Forest Meteorology 197 (2014) 158–168

Contents lists available at ScienceDirect

Agricultural and Forest Meteorology

journal homepage: www.elsevier.com/locate/agrformet

Canopy closure, LAI and radiation transfer from airborne LiDAR synthetic images

D. Moeser[a,*], J. Roubinek[a], P. Schleppi[b], F. Morsdorf[c], T. Jonas[a]

[a] WSL Institute for Snow and Avalanche Research SLF, Davos Dorf, Switzerland
[b] Swiss Federal Institute for Forest, Snow and Landscape Research WSL, Birmensdorf, Switzerland
[c] Remote Sensing Laboratories, Department of Geography, University of Zurich, Zurich, Switzerland

ARTICLE INFO

Article history:
Received 13 January 2014
Received in revised form 27 May 2014
Accepted 10 June 2014

Keywords:
Aerial LiDAR
LAI
Canopy closure
Radiation transfer
Forest snow hydrology
Synthetic images
Hemispherical photography

ABSTRACT

Forest canopy structure and associated solar radiation fluxes greatly influence snow accumulation and melt and have large implications for water availability from forested areas. The ability to efficiently and explicitly infer canopy parameters at high resolution is crucial to improve the success of large scale applications of snow water resources modeling within these areas. In this paper, the utility of estimating leaf area index (LAI), canopy closure (CC) and below canopy potential incoming solar radiation (PISR) from synthetic hemispheric photos derived from airborne LiDAR data was evaluated. LAI and CC estimates from the synthetic LiDAR images were directly compared to actual hemispherical photos taken at 16 points at 7 field areas with heterogeneous canopy stand characteristics for a total of 112 photo comparison points. The synthetic data was further analyzed against LAI and CC derived from more traditional aerial LiDAR methods using a Cartesian space which integrates values over an area rather than a point based angular viewpoint. Furthermore, the PISR estimates were directly compared to in-situ radiometer measurements taken at 30 different locations during clear sky conditions with heterogeneous canopy stand properties. When compared to the actual hemispherical photos, the CC and LAI metrics from synthetic images showed higher correlations and lower biases for all canopy coverage classes (r: 0.93 for CC and r: 0.83 for LAI) than the metrics from the Cartesian approach which displayed decreased correlations and higher biases with increasing canopy closure. Using a clear sky partitioning scheme for the direct and diffuse portions of the incoming shortwave radiation, the PISR was also accurately estimated from the synthetic images with average site correlations ranging from 0.90 to 0.94 where the timing and peak trends of both the diffuse and direct radiation components were well represented. Finally, a basic methodology for the steps toward automation of the process was presented in order to explicitly derive these metrics within similar LiDAR datasets.

1. Introduction

Forested headwaters that are snowmelt dominated produce 60% of the global freshwater runoff (Chang, 2003). Within the Northern hemisphere it is estimated that 20% of the seasonal snow cover is located within forested areas and can account for 17% of total terrestrial water storage during the winter season (Guntner et al., 2007; Rutter et al., 2009). However, the state of forest structures within these zones is changing due to effects from climate change and land use management, as well as a variety of natural disturbances all of which create uncertainty regarding the fate of this major water cycle component. The necessity to better understand the interplay between forest structures and snow is augmented by alarmingly high global water withdrawal predictions ranging from an increase of 18–50% for just 13 years from now in 2025 (Rosengrant et al., 2002).

Arriving at accurate estimations of the variations in snowmelt and runoff rate from forested areas is of great importance to hydrologic forecasters throughout the world. However, accumulation and ablation of seasonal snow cover within forested areas exhibits very different dynamics as compared to snow within open areas (Jonas and Essery, 2011; Pomeroy, 1995). This is due to the surrounding forest structure acting to both exacerbate and diminish involved physical processes, creating much greater spatial snow pack heterogeneity compared to open areas.

* Corresponding author. Tel.: +0041 0 81 4170 156; fax: +0041 0 81 4170 0110.
E-mail addresses: moeser@slf.ch (D. Moeser), roubinek@slf.ch (J. Roubinek), patrick.schleppi@wsl.ch (P. Schleppi), felix.morsdorf@geo.uzh.ch (F. Morsdorf), jonas@slf.ch (T. Jonas).

http://dx.doi.org/10.1016/j.agrformet.2014.06.008
0168-1923/

The multidimensional arrangement of overhead forest canopy characteristics controls a variety of physical under canopy energy and water balance drivers and standard snow modeling approaches integrate both leaf area index (LAI) and canopy closure (CC) (or sky view fraction) to describe the canopy. Conventional direct measurement methods for estimating the overhead canopy structure are severely labor intensive and typically involve destructive sampling of the overstory. However, there are a variety of indirect measurement schemes and their utility is dependent upon the canopy qualifier in question. These indirect field estimations of canopy structure include hemispherical photography, plant canopy analyzers like the LAI-2000, or a spherical densitometer and each have particular strengths and weaknesses depending on the specific structure element (Breda, 2003; Hyer and Goetz, 2004).

Similar to physical canopy structure measurements, field estimations of potential incoming solar radiation (PISR), or a composite of the direct and indirect components of shortwave radiation during clear sky conditions at specific points, can be costly and time consuming and generally necessitate radiometer array deployment around the field area. PISR measurements are variable through space as well as time and can drastically vary on a local level due to the presence of canopy components relative to the sun track. Most commonly, arrays of fixed sensors have been used to capture the spatial variability of radiation below the canopy (Link et al., 2004; Pomeroy et al., 2008). Alternatively, radiation sensors have been moved manually or automatically along ground transects, cables, or rails (Stähli et al., 2009; Sturm et al., 1995). This variation as compared to open areas necessitates measurement of multiple sites making it impractical to use ground-based measurement to estimate the spatial and temporal dynamics of PISR under canopy for large areas. Due to this, many practitioners have used estimates of canopy parameters such as LAI to empirically derive PISR (Hellström, 2000). Hemispherical photographs can also be used, as the photographs serve as records of the geometry of canopy openings in order to determine precisely the PISR as it is related to the surrounding forest architecture (Thimonier et al., 2010; Musselman et al., 2012).

Hemispherical photography (HP) has traditionally been used to arrive at three key parameterizations, LAI, CC and more recently PISR, primarily because their determination is dependent on an angular viewpoint from a point to describe the distribution of multidirectional gap fractions. Despite the proven utility of HP, image acquisition and processing is very time consuming, thus limiting the utility of accurately describing these parameters for large areas. Aerial laser scanning (ALS) data has been increasingly utilized to derive estimates of these descriptors and is becoming more readily available for large areas throughout the world. Most practitioners utilize an area averaging approach where a basic ratio of canopy pixels to total pixels based on an analysis of grid size as well as height cutoff for canopy closure whereupon correlations with hemispherical photos are generally good (Lovell et al., 2003; Riaño et al., 2004).

Many estimates of LAI from ALS utilize a ratio of canopy returns to total echo returns over an area to arrive at a LAI proxy for a point (Morsdorf et al., 2006; Solberg, 2010; Solberg et al., 2009). However these methods do not directly integrate an angular field of view which is why relating these different perspectives creates intrinsic difficulties when comparing the area averaged output to a point based output such as hemispherical photography (Varhola et al., 2012). The downward looking vertical distribution of foliage from ALS and upward looking angular distribution which integrates larger volumes of branches and trunks from hemispherical photography for a point affects an accurate inter-comparison of the two (Fig. 2). Furthermore, these methods necessitate averaging values over larger areas for an individual point implicating a utility directed at area based rather than point based estimates. Several recent studies have converted ALS data from a traditionally Cartesian or X,Y,Z space into a polar system in order to mimic point based hemispherical photographs which are increasingly thought of as the standard for derivation of these parameters (Alexander et al., 2013; Musselman et al., 2013; Varhola and Coops, 2013; Varhola et al., 2012). This new development also allows for a visual as well as quantitative analysis of the output giving a physical basis to LiDAR based approaches as well as greatly reducing the requisite setup and processing time needed to take real hemispherical photos.

This study has created a methodology allowing for direct extrapolation of LAI, CC and PISR from the conversion of ALS into a ground view angular perspective. We have automated the process of explicitly creating LiDAR derived hemispherical photos (synthetic images), and the subsequent parameter estimations (LAI, CC, PISR). We then directly compared these to the parameters derived from hemispherical photos taken on the ground. In order to evaluate the utility of a point based angular perspective, the LAI and CC estimates were further compared with those derived from a standard areal averaging Cartesian approach by utilizing a basic form of the methods highlighted in the works of Essery et al. (2008), Fleck et al. (2012), Morsdorf et al. (2006) and Solberg et al. (2009). Finally the PISR estimations were then directly compared to a series of ground based radiometer arrays in various canopy and topography regimes. This is the first study of which we are aware, that has employed such techniques with (1) high resolution data over (2) large domains with (3) spatially explicit ground truth data at a large number of points within diverse canopy coverage areas (1862 points available for direct ground comparison).

2. Methods

A series of 7 forested field areas have been established for long term study in the region immediately surrounding Davos, Switzerland (Fig. 1). Each field area was 50 m by 50 m and was located within three generalized elevation (low to high: Laret, Drusatcha, Ischlag) and canopy coverage (low, med, high) classes. Despite the generalized CC classification, each field area exhibited heterogeneous canopy coverages at the sub-plot scale (Fig. 1) allowing for a multi-scale analysis on a broad range of canopy classes. Field areas are characterized by low to no surface slopes with low surrounding terrain shading influences. Forest stands were predominately Norwegian spruce and varied in height from new growth up to 45 m in height with the majority between 10 and 30 m.

Field areas were set up in the fall of 2012 and are part of a long term forest snow hydrology study area operated by the WSL Institute for Snow and Avalanche Research (SLF). A distometer (Leica Disto X310) was used to calculate accurate (±1 cm) 10 m intervals for the positions of 36 intersection points at each field area, which were then marked with 2.4 m long poles. A nylon cord was fixed between all pole intersection points and 2 m intervals were manually measured and marked along each of the six north–south and six east–west transects for a total of 276 points per site. A differential GPS (Trimble geo XH 6000) was used to arrive at coordinates of each internal pole point with a maximum error of ±20 cm. These coordinates were then distributed to all 2 m interval points with an estimated rectification error of ±50 cm. This gave a total of 1862 geo-referenced locations available across all field areas for direct ground comparison.

2.1. Hemispherical photos

Hemispherical photography utilizes a lens with an extremely short focal distance allowing for a broad field of view of approximately 180°. The field of view limit, with the camera directed upward, can reach the horizon and for processing purposes each

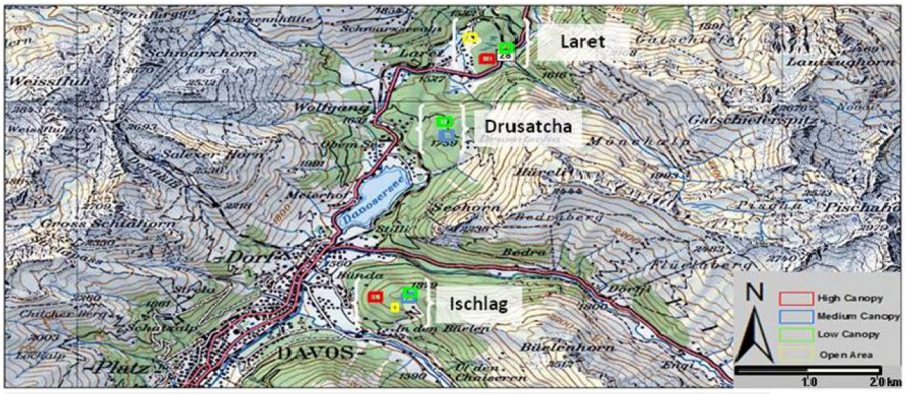

Field Area	Elevation	Canopy Coverage			
		Low	Med	High	Open
Laret	1546	√	x	√	√
Drusatcha	1764	√	√	x	x
Ischlag	1874	√	√	√	√

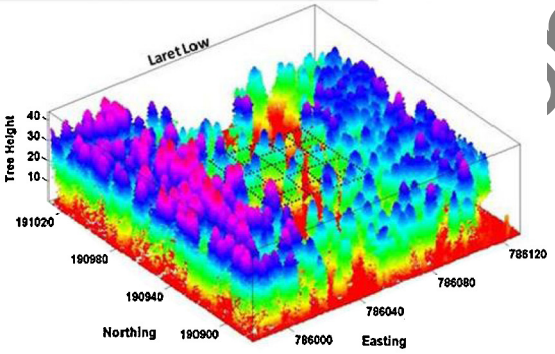

Fig. 1. The study areas are located in various elevation bands and distinct canopy coverage regimes surrounding Davos, Switzerland. The green forested areas in the upper map represent the majority of the LiDAR dataset extent. The lower right box plot is a digital representation generated from the raw LiDAR data of the 'Laret low' field area with the geo-rectified sampling grid inside (276 points). The remaining 6 field sites have the same design setup. A hemispherical photo was taken at each internal grid crossing for a total of 16 photos per site as well as 10 auxiliary locations at three sites for the radiation measurement campaign.

point within the horizon's projected circle is defined by polar coordinates. The image angle corresponds to the azimuth, and the radius indirectly corresponds to the zenith angle. We took 16 hemispherical photographs at all primary intersection points within each field area for a total of 112 photographs (Fig. 1). The photos were taken using a Canon 600D with a Sigma 4.5 mm F2.8 EX DC HSM circular fisheye lens mounted on a specifically designed tripod allowing for quick leveling and directional setup to true north. Each photo was taken 1.2 m above the ground surface in May 2013 under primarily low light conditions in order to maintain a good sky-canopy contrast. Underexposed photos were taken to get good contrast between the canopy and the sky. A point exposure measurement of the sky was first taken and this value minus 0.5 exposure stop was utilized for the setting.

2.2. Airborne LiDAR data

LiDAR data acquisition was carried out from the 11th to the 15th of September 2010 using a Riegl LMS Q 560 sensor from a series of helicopter flyovers at a nominal flying altitude of 700 m for a total area of ~90 km^2. The wavelength emitted from the Riegl device was 1550 nm with pulse durations of 5 ns and includes up to 7 returns per pulse with a maximum scan angle range of ±15°. The average point density of the full waveform data set yielded an average echo density of 35.68 m^{-2} of the flyover domain and 19.05 m^{-2} for the last returns within the utilized domain area. The affiliated digital terrain model (DTM) or the underlying ground surface elevations were computed by using the classified ground returns at a 0.5 m horizontal resolution by Toposys using their in house processing software, TopPit (http://www.toposys.com/).

2.3. Radiometer installation

An array of 10 radiometers (CM3 pyranometers: Kipp & Zonen) which measure the sum of direct and indirect shortwave radiation were deployed for 24 h intervals at three field sites: Laret low, Drusatcha medium and Ischlag high. All sites demonstrate low terrain shading and are located at three elevation and canopy closure regimes (see Fig. 1). Each radiometer was fixed approximately 10 m to the north, south, east, west, northwest, northeast, southwest, and southeast, respectively, from a center point, which was also equipped with a radiometer. The final or tenth radiometer was set within a canopy closure regime that was not captured with the others. The circular array was set in a specific position within each of the three field areas to capture as much canopy heterogeneity as possible while retaining a generalized canopy regime representative of the entire site. Like the predefined site grids, all points have been geo-referenced and an affiliated hemispherical photo was taken at the exact point where each radiometer was placed. Each campaign was carried out during 100% visual clear sky conditions from sunrise to sunset on the 14th of August 2013 for Drusatcha medium, 22nd of August 2013 for Ischlag high and the 3rd of September 2013 for Laret low. The 15 s output format from the radiometers were then aggregated for 10 min intervals.

2.4. Polar coordinate conversion

In order to incorporate a point based angular viewpoint into LAI, CC and PISR calculations, raw ALS data was converted into a spherical coordinate system where the traditional Cartesian coordinates, X, Y, and Z were converted into a distance from the origin to the point (R), the inclination or polar angle between the zenith and a projected ray from the origin to the point (θ, theta) and the angle between the positive x axis and the x/y plane (Φ, phi). A significant amount of pre-processing was initially required in order to use the point cloud data and represent this data as hemispheric images. All holes within the DTM (terrain surface below the canopy) were first filled using a triangular based interpolation. Elevations from the raw data were converted into canopy heights by taking the difference between the raw point cloud elevations and the

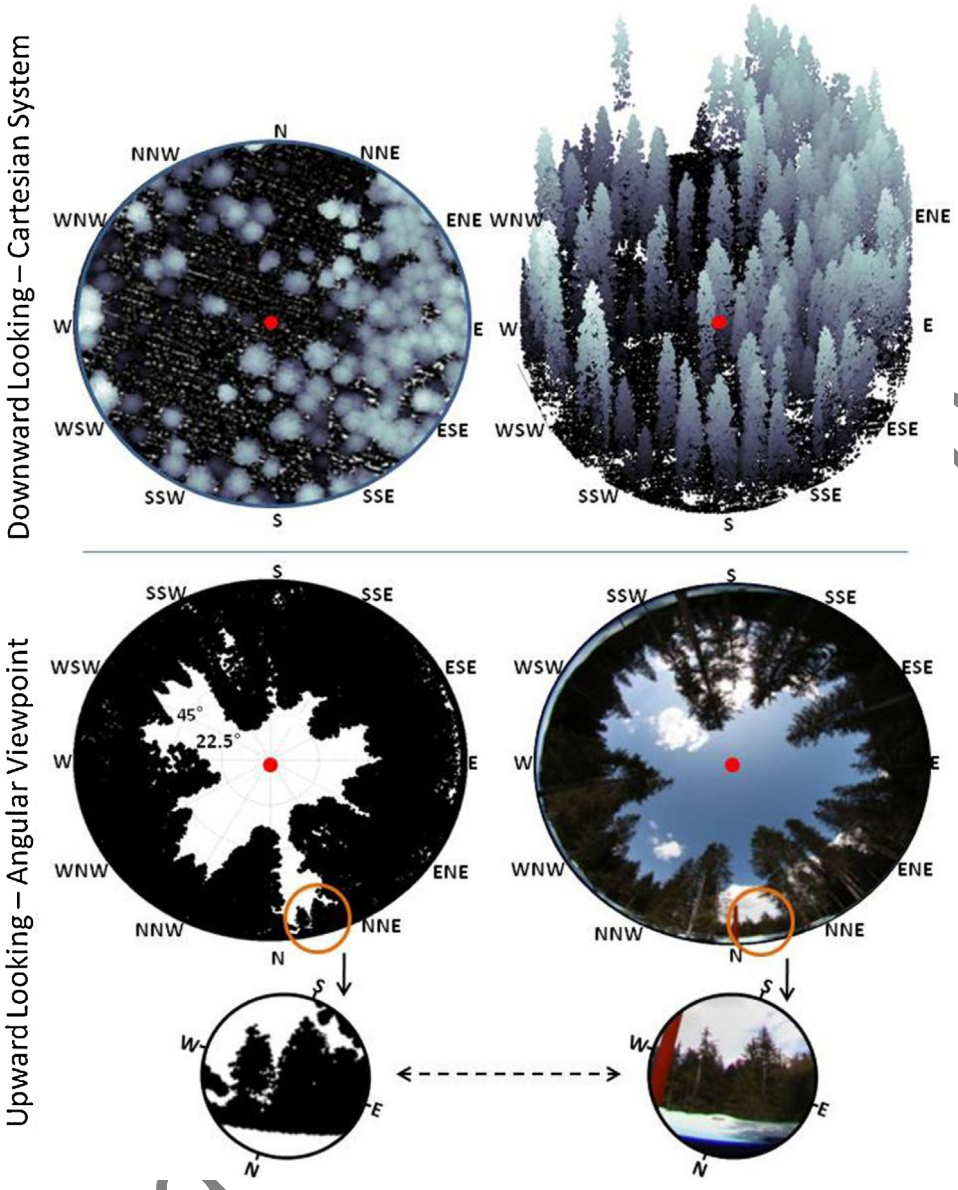

Fig. 2. The standard overhead Cartesian viewpoint from the LiDAR is displayed on the upper tiles. The lower tiles are representations of an angular viewpoint where a hemispherical photo is displayed on the right and a synthetic hemispherical image (Polar projection system) on left with distance integrated pixel print size. Canopy points closest to the origin are represented as large pixels and points further away as small pixels. Bottom images are zooms of canopy characteristics on the horizon. All images are from the same point (Laret Low field area) and integrate a data trap size of 100 m. The point of acquisition is labeled as a dot in the middle of each image. Note the large geometric projection differences between the Cartesian system (upper tiles) and the polar system (bottom left lower tiles).

DTM. Any canopy heights below 1.2 m, representing the acquisition height of the hemispherical images, were removed. Φ was calculated from 0 to 90° for a full 180° view frame. The θ values were then flipped on the east-west to mimic the upward viewing projection of hemispheric photos. Despite some prior work demonstrating that inclusion of data with distances greater than 50 m accounted for no significant correlation increases, no data with horizontal distances less than a 100 m distance from the origin were removed in order to ensure all relevant information is preserved regardless of site specific vegetation heights (Alexander et al., 2013). Polar coordinate plots (as an example, see Fig. 2) were then created at (1) all points where hemispherical photos were taken within the field areas and (2) at all points on each sampling grid per site (1932 points) and saved as image files.

Successful imitation of hemispherical images required several assumptions regarding point size output of the synthetic images. An initial analysis was performed which explored how to introduce distance into the images, i.e. how should a tree at the maximum horizontal distance limit (100 m) be compared to a tree seen near the origin. Several varying point projection algorithms were created for the data set, including (1) a fixed output point size, (2) variable output size based on horizontal distance to point and (3) variable point output size based on distance to point. The optimal output was determined by a sensitivity analysis which was optimized by comparing the correlation between effective LAI as well as CC from the synthetic and real images. The best fit was obtained by distributing the point cloud output into a printed circle with the size directly based on the distance from origin (R). The print size of the circle was linearly interpolated from near to far (Fig. 2, lower left tile). The process was automated allowing for almost immediate production of 112 synthetic images at the exact coordinates as the actual images as well as production of images at each of the labeled points within the 7 field areas for a total of 1932 synthetic hemispherical images. This process has also been created to

facilitate extension to other data sets in order to explicitly arrive at synthetic hemispherical images within an ALS dataset domain based solely on a coordinate input list.

2.5. Estimation of LAI and canopy closure with an angular approach

The HP and synthetic photos were analyzed by 'Hemisfer', version 2-beta, an image analysis software developed at the Swiss Federal Institute for Forest, Snow and Landscape Research WSL (http://www.wsl.ch/dienstleistungen/produkte/software/hemisfer/, Thimonier et al., 2010). This software was used to obtain effective LAI, CC and PISR. These calculations are based on the classification of pixels as either white (sky) or black (canopy) by applying a brightness threshold to the analyzed picture. Thresholding of real photographs was carried out according the algorithm of Nobis and Hunziker (2005) integrated in Hemisfer, taking into account the gamma value ($\gamma = 2.2$) of the pictures. In some pictures (dependent upon the contrast) the blue color channel was used in order to improve the contrast between the sky patches and the vegetation. Light transmission, T, was then calculated as the proportion of white pixels within analysis rings, with the rings defined as ranges of zenith angles θ (theta) in 15° steps. The contact number, K, or average number of times that a straight line would touch the canopy over a distance equal to the thickness of the canopy was calculated as a function of the zenith angle and light transmission:

$$K = -\cos\theta \ln T \quad (1)$$

The K values were then integrated over rings of various θ angles to obtain effective LAI in accordance with a standard technique first introduced by Miller (1967). No clumping correction was applied (for the sake of simplicity LAI represents effective LAI within this paper). Canopy closure was calculated as the average of the $T(\theta)$ values, weighted by the solid angles of the corresponding rings.

2.6. PISR

The potential incoming solar radiation under the canopy (PISR) was calculated from analysis within the Hemisfer program with the transmission of the direct and diffuse components through the canopy structure represented by each real or synthetic picture. Modeled clear sky and real sky conditions were utilized to partition the atmospheric direct and diffuse radiation parameters. While the clear sky conditions better mimic potential incoming solar radiation it was also necessary to include a 'real' sky condition when estimating solar radiation over larger time scales when specific diffuse and direct parameterizations are variable. To partition the real sky conditions over the whole year the average values specified by Timofeev and Vasil'ev (2008) were used where the direct and diffuse radiation parameters were set to 25% of the solar constant. The clear sky conditions specific to the field areas as well as our radiometer campaign dates were utilized and made available at 15 min intervals from the photovoltaic geographic information system project (PVGIS) within the European commission joint research center, Institute for Energy and Transport (http://re.jrc.ec.europa.eu/pvgis/solres/solres.htm, Huld et al., 2008)). This time series was further interpolated to match the 10 min output data of the radiometers.

The calculations within Hemisfer were carried out in 1-min steps according to the position of the sun in the sky, taking the slope and exposition of the plots into account (Schleppi and Paquette, 2014). PISR values obtained for a period ranging from January first to December 31st and were aggregated per 10 min time step. The estimated PISR values from the real and synthetic images on the corresponding day of the radiometer campaign were utilized for direct comparison to the radiometer measurements.

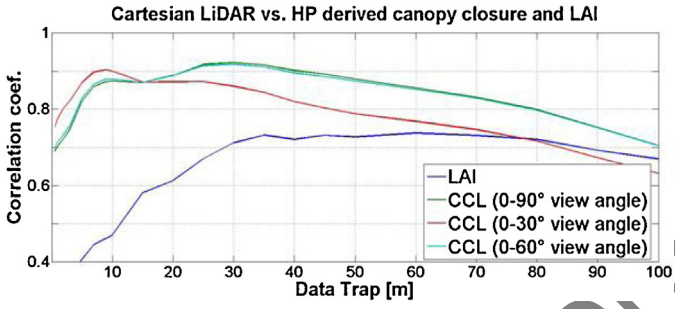

Fig. 3. Correlation between HP and LIDAR (Cartesian coordinate system) derived LAI and CC. Varying data trap sizes of the aerial LiDAR data were utilized and analyzed for correlation to the HP values. Three viewing angles from 0 to max or 90° within the HP data, representing the differing zenith angles of the hemispheric photos were also compared with the CC derived from the Cartesian system. The best correlation is for a 90° viewing angle with a trap size of 30 m for CC, while LAI necessitated a slightly larger data trap of 35 m for the best correlations.

2.7. Estimation of LAI and canopy closure within the Cartesian system

Effective LAI and CC were also calculated from the raw ALS data without a coordinate transformation and used as comparative tool for the estimates from the synthetic images. Canopy closure was calculated by first converting all returns from the point cloud into a 0.5 m grid and then quantifying the ratio of cells which have canopy cover to the total number of cells within the digital surface model. A LAI proxy was estimated by computing the ratio of all raw LiDAR first returns to total ground returns and was derived from a modified routine initially utilized by Morsdorf et al. (2006) and recommended within the ICP manual for methods and criteria of forest monitoring which analyzes LAI as a ratio of return hits (Fleck et al., 2012; Morsdorf et al., 2006; Solberg et al., 2009). Both metrics were calculated using a height cut-off and a data trap area, where the height cut-off is preset to the height of the field collected hemispherical photos (1.2 m). In this case, the data trap size represents the distance away from the analyzed point with the point located in the center. The data trap was initially left flexible where a sensitivity analysis of the CC and LAI output from the hemispherical pictures were compared to the ALS data and optimized based upon correlation between the datasets (Fig. 3). Estimating parameters in this manner does not utilize a point based angular viewpoint, compared to estimates from a HP approach, (Fig. 2) creating difficulties in direct comparison of both methods. If the data trap is sufficiently small, then only canopy cover, which is a measure of canopy from a specific ground point to the matching overhead point, not canopy closure values can be derived. Canopy closure values however are a measure of canopy from a point to an area (Fiala et al., 2006). Due to this viewpoint discrepancy, CC values were also derived from the HP at three different zenith windows: 0–30°, 0–60° and 0–90° for comparison (Fig. 3). Fig. 3 represents the initial sensitivity analysis which demonstrated that the full frame of view available from HP (0–90° from the zenith) delivered the best results when compared with LiDAR derived CC and LAI output from an analysis bounding box size of at least 30 m. The correlations slightly dropped when smaller viewing angles from the HP's CC derivation were analyzed. The optimal data trap size for LAI, however, was slightly higher at 35 m. The correlations for both parameters, but especially for LAI, were low with small data bin sizes and not until the data trap sizes increased significantly were reasonable correlations seen. However this range will always depend on both the vegetation density as well as the vertical canopy height at each site

(Morsdorf et al., 2006). This range also depends on the line of site obstruction of data as viewed from hemispherical photos. These occlusions can be seen within Fig. 2, if the top left and bottom left panels are compared. The visual scale inequalities between the two systems (Cartesian and polar) also highlight the data representation differences. The differences emphasize the utility of the Cartesian system may be better suited for spatial averages where point estimations are better relegated to an angular or polar approach. Only the estimates of LAI and CC garnered from the optimized bounding box sizes were then used as a comparative tool for the results from the synthetic hemispherical images. As with the parameter investigations in the polar coordinate system, all aspects of the analysis have been automated and can be extended to other LiDAR data sets.

3. Results and discussion

3.1. Synthetic image LAI and CC derivation vs. hemispherical photographs

The sensitivity analysis of the printed point size distribution within the synthetic images was optimized and gave a best fit when a linear interpolation utilized a point size distribution of 7 to 0.5, where the closest points were given a print output of 7 and the farthest points were given a point size of 0.5. As seen in Fig. 4, LAI and CC from the synthetic images showed good correlations and low bias when using this interpolation scheme. Results of this run gave correlation coefficients of 0.83 and 0.93, respectively, when compared to HP output. The correlations remained high for the extent of the series which range from very open areas to extremely closed forests with LAI values ranging from ~1 to 7. Fig. 5 gives a series of examples of HP and synthetic photos at different canopy closure regimes, ranging from 0.75 to 0.96 within 3 distinct field sites. Due to the small size of the images, it is hard to visualize small canopy scale correlations from the point size distribution, but trends within the different gaps sizes are clearly visible. For a visual overview of smaller scale correlations see Fig. 2.

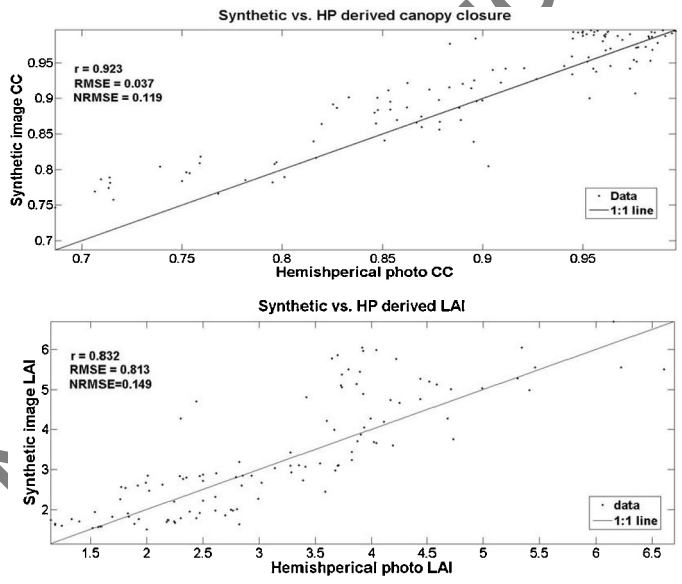

Fig. 4. The upper graph compares CC derived from synthetic images on the *y* axis with HP calculated CC on the *x* axis. The lower graph compares LAI derived from synthetic images on the *y* axis with HP calculated LAI on the *x* axis. The 1:1 line is displayed on both graphs as a solid line. Both metrics display good correlation between methods with correlation coefficients of 0.92 and 0.83 and normalized RMSE's of 0.12 and 0.15, respectively.

3.2. Cartesian system LAI and CC derivation vs. hemispherical photographs

CC and LAI derived from the Cartesian system also provided reasonable correlations between the data series. Correlations of CC derivation in the Cartesian system (*r*: 0.91) were within 1% of the estimated CC correlations from the synthetic images (*r*: 0.92). LAI estimation correlation was 0.73 for the series and represented a 10% reduction when compared to the correspondence between the synthetic and HP images (*r*: 0.83). The CC estimates functioned reasonably well through the entire series from low to high canopy cover values. The LAI estimates also functioned reasonably well, but only on the lower end of the range (LAI ≤ 4). When HP LAI values were greater than 4, the Cartesian derived estimates became saturated and failed to estimate higher values (Fig. 6). The greatest differences, however, did not reside with the correlation coefficient values. All values were systematically biased and necessitated a basic regression correction to arrive at the correct values. This bias has been seen in prior studies and can be manipulated based on the return echo utilized. However the interplay between return echo and CC bias is still unclear because it depends on the sensor used, the underlying vegetation and the echo detection method (Morsdorf et al., 2006). Due to this ambiguity all return echoes hitting above the height threshold (height at which the hemispheric photos were taken) were utilized. ALS data in this system provided a nearly vertical downward view and the offset of the CC values also highlighted the inherent differences in comparing a point based angular derived output with that of a area averaged planar one. Despite the integration of large data traps (as described in Section 2.3.4), which indirectly integrated an angular approach, it is clear that it was still not sufficient when comparing the results to an angular one. The LAI proxy estimates on the other hand were estimated by directly analyzing the ratio of initial returns (which represents outer canopy hits) to total ground returns. This proxy ratio will always be offset and necessitate local scaling to agree with the HP values. The non-linear distribution of these echoes also affected the estimation power of the dataset at higher LAI values due to saturation effects of the echoes (Fig. 6 lower panel).

While forest metric processing in the Cartesian system from this data set display clear advantages over HP use in terms of time consumption and the ability to explicitly arrive at metrics for large areas, its utility and performance was still reduced when comparing this to the synthetic image processing. Specifically, Cartesian based LAI estimation gives no visual output aid to qualitatively asses the output and, at least with this dataset, difficulties arose when calculating LAI within dense forest areas (LAI > 4). Both LAI and CC necessitated a scaling factor to compare with HP output whereas the synthetic images could be directly optimized from the point size output manipulation. The synthetic images allowed for a visual record of the geometry, where at a quick glance one could get a good idea of the overlying forest structure for various points. LAI and CC were estimated with higher precision for the entire data dataset range as compared with the Cartesian approach. These differences imply that the point LAI and CC estimations are better estimated using a polar system whereas the utility of the Cartesian system may be better suited for spatial averages.

3.3. PISR comparison

PISR was initially calculated from the HP and synthetic images within Hemisfer by adding both the diffuse and indirect shortwave radiation components. The 10 synthetic images per site were parsed into 10 min and 1 h time step averages. This data was then used to directly compare with the 24 h of data from the radiometer

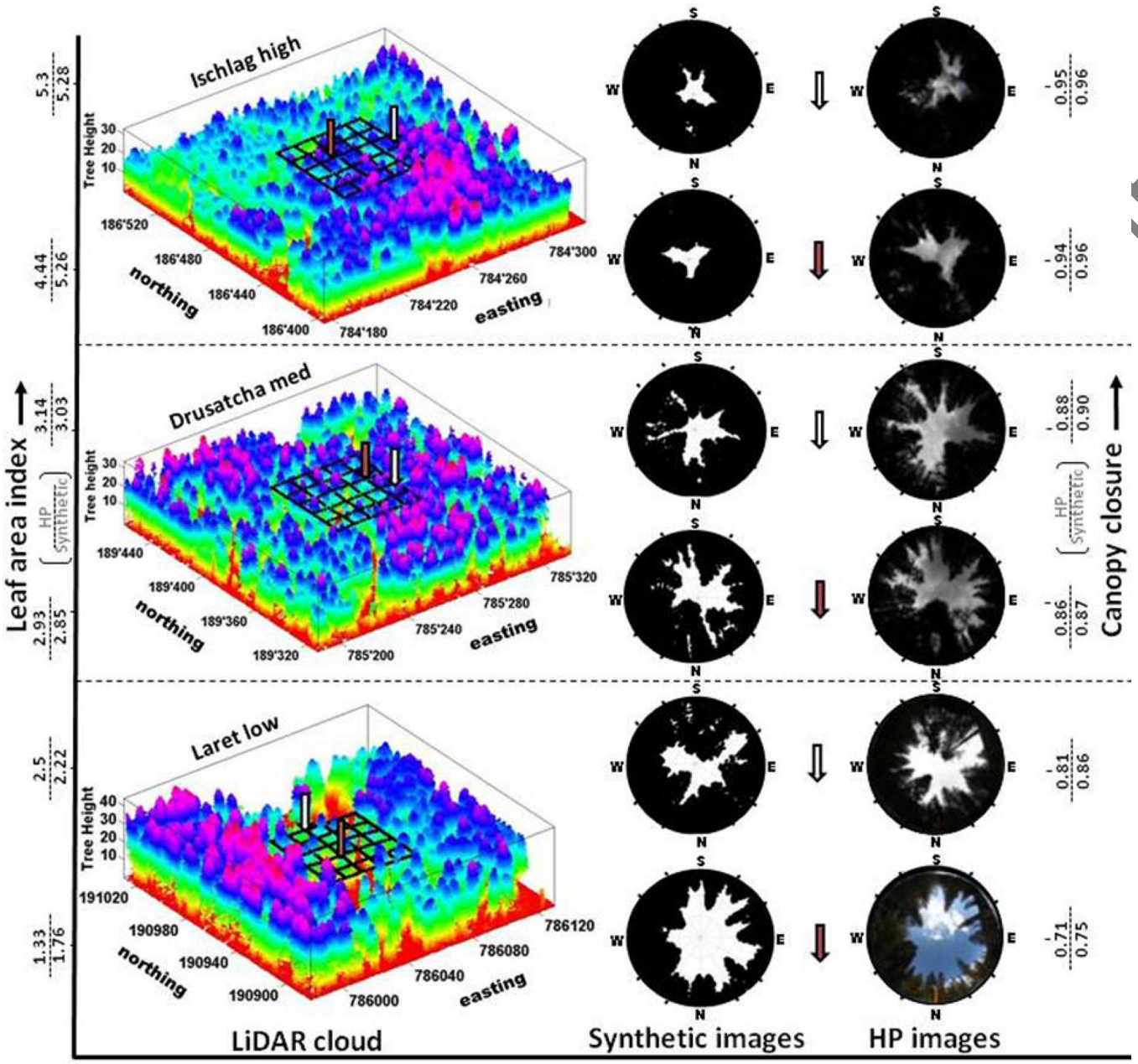

Fig. 5. Examples of synthetic images from three field sites representing low canopy, medium canopy and high canopy closure (in the middle column) which range in LAI from 1.76 to 5.28. The *y* axis increases in canopy closure and LAI values with the top number being values calculated from HP and the lower number being estimations from the synthetic images. The left column contains LiDAR data cuts of 150 × 150 m for three field areas from low to high canopy cover. The internal black lines represent the sampling grid (50 × 50 m) where the hemispherical photos were taken. On the grid, two arrows represent the synthetic and HP locations. The right column holds the hemispherical photos.

campaigns for (1) individual radiometers as well as (2) field site composites (average of 10 radiometers per site).

The field site composite comparisons of the synthetic and radiometer data show correlation coefficients ranging from 0.90 to 0.94 at 1 h time steps and 0.73 to 0.83 for 10 min steps with similar correlations seen within the HP photos (Table 1). The individual point comparisons using the synthetic images gave average correlations of 0.72 for the 1 h data series and 0.51 for the 10 min data. Fig. 7 shows three individual point comparisons at varying canopy cover regimes at 10 min intervals within each of the radiometer campaign sites where the correlation ranged (from the synthetic images to radiometer measurements) 0.70 to 0.88 with an average normalized RMSE of 0.264. The general timing and peak trends of PISR was well represented within the 10 min synthetic data series at the point scale. However the bias of the direct radiation component increased with increasing canopy closure values canopy (starting at CC values of 0.85), and caused a reduction in peak radiation estimation within the synthetic images which had CC values ≥0.85. This was readily apparent at the high canopy density site, Ischlag high, where the direct component of solar radiation was not fully captured (Fig. 7 top graph). The HP series also demonstrated similarly good correlations; however the goodness of fit showed no link to increasing canopy closure. Fig. 9 column 'a' show site comparisons of synthetic data at hourly time steps. This data also captured the timing and peak trends of both the diffuse and direct shortwave radiation component at all sites, but like the point data series, the Ischlag high field sites demonstrated a reduction in the direct component correlation

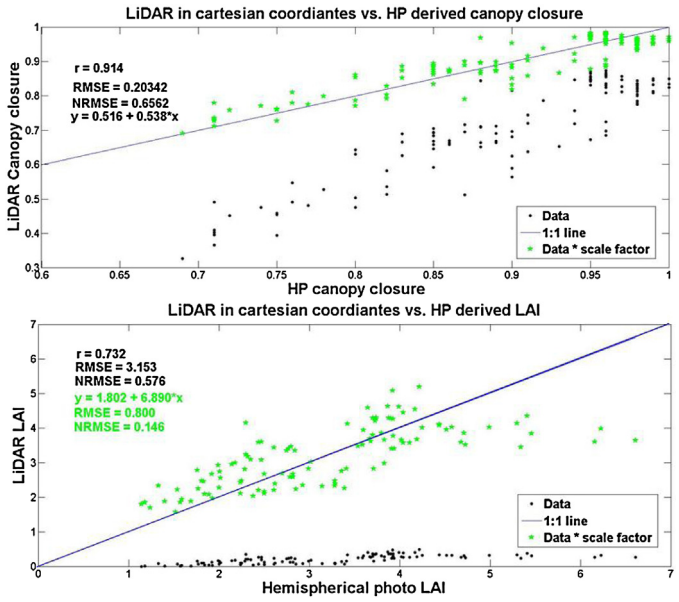

Fig. 6. The upper graph compares canopy closure derived from LiDAR in the Cartesian system on the *y* axis with HP calculated canopy closure on the *x* axis (black). The correlation is within 1 percent of that of the values derived from synthetic images. However the values are systematically biased necessitating a basic regression to obtain comparable estimates (grey). The lower graph compares LAI derived from LiDAR in the Cartesian system on the *y* axis with HP calculated LAI on the *x* axis (black) where the correlation is 10 percent lower as compared to that of the values derived from synthetic images. A basic regression is also necessary to arrive at comparable values (grey). The LAI correlation with this approach also degrades with values above 4. In both charts, the black dots represent the initial estimates and the green stars represent the regressed values.

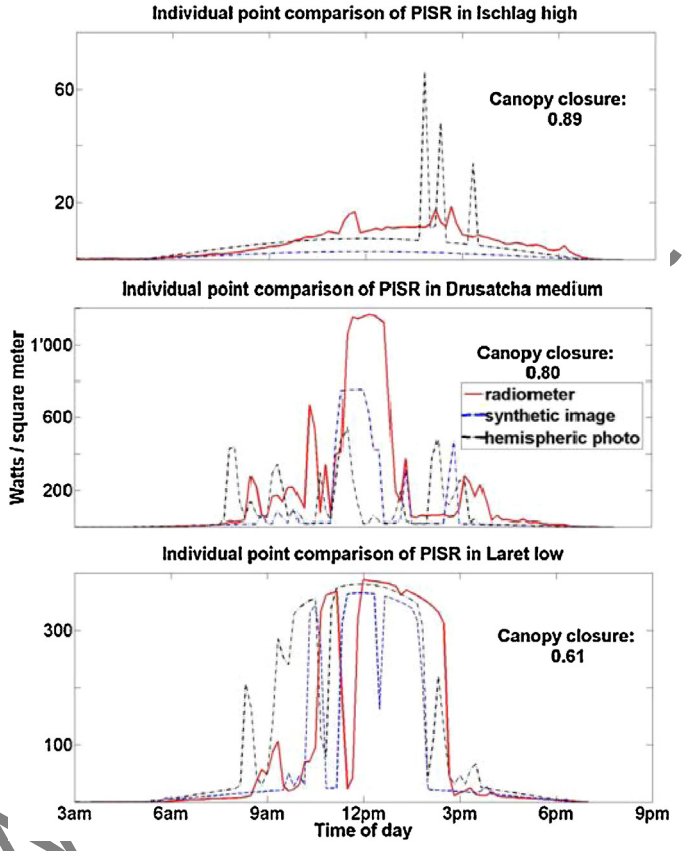

Fig. 7. Comparison of 10 min average radiometer (red), hemispheric photo (black) and synthetic image (blue) data for individual points with different canopy closure values. From low to high: (1) Laret low (2) Drusatcha med and (3) Ischlag high field areas. The modeled data utilized the PVGIS direct and indirect shortwave radiation partitioning for clear sky global irradiance in Davos Switzerland for the radiometer campaign dates. (For interpretation of the references to color in this figure legend, the reader is referred to the web version of this article.)

with the radiometers. The data fits maintain high correlations, but the comparisons demonstrated increasing biases (Fig. 8) with increasing canopy closure as previously described with the point comparisons.

Calculations of total offset of estimated PISR from the synthetic images to the radiometer measurements at all points (total of 30) were plotted against canopy closure (also calculated from the synthetic images) and an exponential relationship was defined between the two when canopy closure values increase above 0.85. See Fig. 8. This relationship was then applied to the field estimations seen in column 'a' of Fig. 9. The same comparison was made utilizing the HP data series and a similar trend between the offset of modeled and observed PISR vs. canopy closure was seen until the closure values increased above canopy closure of ~0.85, where no rising limb was seen. Since this exponential relationship was not visible within the HP photo data series, it seems likely this offset within some of the synthetic images was due to the thick cover integrated into the synthetic images as overlapping pixels which reduced simulated solar beam transmittance. While the point size distribution worked well for the duration of the data series for CC and LAI, it is hard to avoid overlapping pixels at not just dense areas but also at the perimeters of the pictures. Even though smaller pixels were assigned to these distant points, the high amount of returns within dense canopy can falsely remove small gaps within the canopy. However, the predefined linear point size distribution size (see Section 2.4) did not seem to be the only constraining factor. The simulations from the hemispherical photos showed no reduction in bias at the high density sites but a small decrease in correlation with increasing canopy cover. This is hard to decipher because the radiometers utilized did not separate the diffuse and direct portion of the radiation creating difficulty in a full analysis of the PVGIS modeled clear sky portioning scheme utilized in

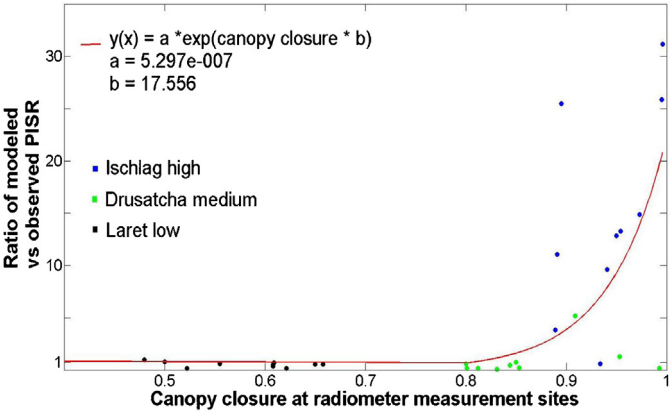

Fig. 8. The offset of PISR estimations from the synthetic photos to the radiometer measurements (*y* axis) were plotted as a function of canopy closure (*x* axis). Site locations of each of the 10 radiometer points are labeled with different colors. As canopy closure increases beyond 0.85 an exponential relationship was used to describe the interaction between ratio and canopy closure (red line). A value rescaling algorithm was created from this relationship and applied to all synthetic photos at each field site. (For interpretation of the references to color in this figure legend, the reader is referred to the web version of this article.)

Table 1
Correlation coefficients, RMSE's and normalized RMSE's of all radiometer measurements as compared to the estimated values from (a) HP photos, (b) synthetic images and (c) synthetic images with a rescaling function at each radiometer campaign field site. The values in bold are from 1 h composites and the values in dark grey are from 10 min averages.

(1 h avg/10 min avg)		*R*	RMSE	NRMSE
Laret low	HP photos	**0.918**/0.823	**67.52**/103.04	**0.147**/0.21
	Synthetic images	0.897/0.784	84.00/114.70	0.449/0.415
	Synthetic images with rescaling function		80.93/113.00	0.176/0.225
Drusatcha medium	HP photos	**0.922**/0.858	**43.59**/60.24	**0.124**/0.149
	Synthetic images	0.942/0.833	58.26/73.22	0.85/0.736
	Synthetic images with rescaling function		41.27/68.01	0.118/0.168
Ischlag high	HP photos	**0.84**/0.636	**8.163**/14.36	**0.263**/0.197
	Synthetic images	0.898/0.739	14.622/95.77	0.528/0.131
	Synthetic images with rescaling function		5.354/15.91	0.163/0.237

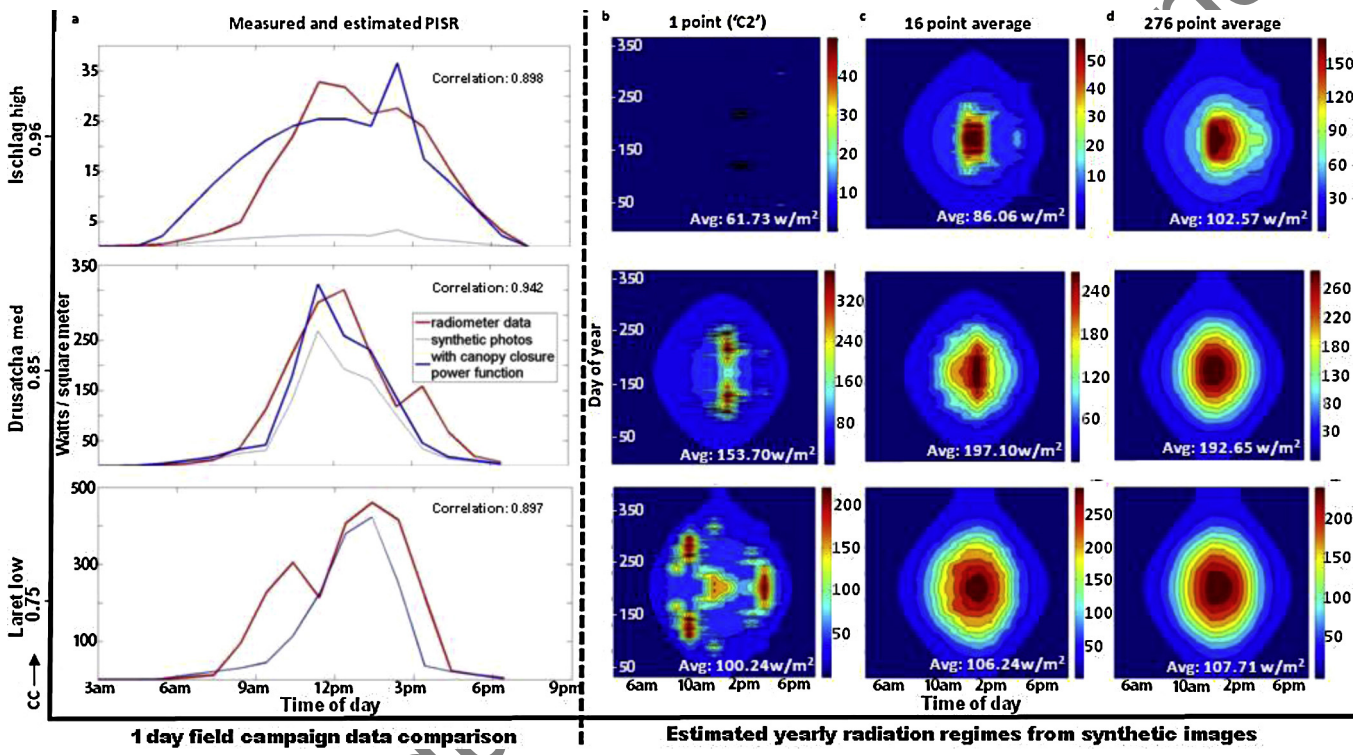

Fig. 9. The *y* axis represents data from low to high canopy closure with average field site values seen beside each field area name. Column (a) shows a direct comparison of average hourly values from the 10 radiometers (red) at each field site and the estimated values from the 10 synthetic images (thin blue) as well as a value rescaling algorithm (thick blue) as a function of canopy closure applied to the initial estimates which had canopy closure values greater than 0.85. The initial estimates utilized the PVGIS direct and indirect shortwave radiation partitioning for clear sky global irradiance. The correlations between the synthetic photo estimates and the radiometer values can be seen in bold. The subsequent columns ((b)–(d)) shows estimated yearly radiation regimes from the field areas (w/m^2) derived from synthetic images utilizing the generalized radiation partitioning values from Timofeev and Vasil'ev. Column (b) is an estimation from one point (at the approximate center of field area—point C2). Column (c) is an average of 16 values from all primary intersection points within each field area. Column (d) is an average of 276 values from all sampling points within each field area. Average daily values can be seen in white where values are calculated from sunrise to sunset. Note the discrepancy within values lending emphasis to high resolution data extrapolation.

the radiation partitioning. Nonetheless, the predictive power of the HP and synthetic photos maintained a good fit and necessitated no scaling function for any points with canopy closure below 0.85.

Yearly synthetic PISR estimates were also derived for (1) all points within each sampling grid of the solar radiation field areas, 276 points per site (276/(50 m)^2), (2) at all primary intersection points within each field area, 16 points per site (16/(50 m)^2) and (3) at the center of each field area (1/(50 m)^2). In these cases, the generalized real weather direct and diffuse radiation partitioning coefficients from Timofeev and Vasil'ev (2008) were utilized. These factors do not give a clear sky condition like the time series data from the PVGIS model utilized within the direct radiometer comparisons. Instead, they give an average partitioning value and are thus more accurate over time. The yearly under canopy PISR estimations ranged from ±8% to ±78% between scales (1/(50 m)^2 : 16/(50 m)^2 : 276/(50 m)^2) with an average scalar difference of approximately ±50%. The results can be viewed within Fig. 9 as a yearly radiation regime along with the yearly averages displayed on each graph. This demonstrates the extreme variance of radiation regimes underneath forest canopy and emphasizes the necessity of explicit radiation regime estimates at fine scales.

4. Conclusion

LAI and CC could be accurately predicted at high resolution and low bias across all canopy coverage conditions using the synthetic

images and displayed several improvements over that of the Cartesian system estimations when using this data set. The synthetic images were able to estimate both metrics from low to high generalized canopy coverages where the standard Cartesian coordinate system (with our approach) was not able to effectively predict LAI at values above 4. The synthetic images also allowed for an initial visual analysis to qualitatively analyze the validity of the estimated metrics as well as allow for a visual comparison to hemispherical photographs. The Cartesian system demonstrated universal biases of estimations and required a basic regression to arrive appropriately scaled values. Furthermore, this bias correction was still not able to accommodate for improved accuracy of LAI values above 4. The synthetic images demonstrated improved correlations and normalized RMSE's for both canopy metrics (r: 0.93 for CC and r: 0.83 for LAI) and required no data scaling. Scalar inequalities (Fig. 2) between the Cartesian system, where canopy elements are averaged over an area, and the point based polar system integrate canopy components in different manners. These differences can be seen within the results and imply that the LiDAR integrated with Cartesian system may be better relegated for spatial averages whereas synthetic images from LiDAR data may be better suited for point estimations.

Both methods can be utilized with different datasets; however production of synthetic images will require a re-analysis of the point size distribution if datasets with a different average echo density are utilized as this is an indirect function of the overall density of the LiDAR dataset. It is possible that future work can integrate point cloud density into point size distribution for a general scaling function for all data sets. However, it should be cautioned that with less dense point clouds more thought is needed to arrive at a distribution due to the non linearity between the landscape and the photo output when using a hemispherical lens Schleppi et al. (2007). This suggests that for a general point size distribution equation to be formulated, focal length must also be integrated into the distribution function for lower resolution data sets. Integration of the LiDAR return type may also prove to be an important factor in creating a universal point size distribution. Despite this initial hurdle, when the appropriate point size distribution was found, this method was able to predict LAI and CC over the entire dataset domain across all possible canopy density conditions without a subsequent regression to account for the scaling or estimation differences.

PISR was also precisely estimated from the synthetic images with average site correlations ranging from 0.90 to 0.94. This method allowed for flexible direct and diffuse incoming radiation partitioning dependent upon the day and point in space analyzed. However at canopy closure values greater than 0.85 the direct radiation component was underestimated from the synthetic images and necessitated an exponential scaling function based on canopy closure. This emphasizes the need for extended research regarding an improved method for scaling the printed point size distribution of the synthetic images in order to resolve the need for a canopy density based scaling function to better transfer these methods to other LiDAR datasets with non-concurrent point cloud sizes.

Despite potential problems with automatic transference of the results to other datasets, the results prove to be extremely promising for high resolution derivation of canopy and solar radiation metrics. The ability to accurately infer these parameters explicitly on very small scales has major implications for snow modeling within forested areas. Canopy interactions and solar radiation under the canopy influence snow cover, snow depth and snow density at sub-m scales. This small scale heterogeneous behavior creates intrinsic difficulties when forest snow processes are generalized within larger scales. A good example can be seen in Fig. 9 where average PISR values at three different field areas are derived for a point, and for an ensemble average of 16 and 276, respectively. The major difference between these values (±8% to ±78% differences with an average of ±50%) highlights the need for explicit high resolution parameter estimation within heterogeneous canopy coverages. The ability to model these factors for any point where LiDAR data of sufficient resolution is available can allow for better parameterizations of forest snow mass and energy balance models. This can permit more detailed analyses of large scale forest snow hydrological issues that were previously impossible before the availability of such datasets.

Acknowledgments

This project was funded by the Swiss National Science Foundation (SNF) (project 200021_146184/1). Substantial field help and support was given by Clare Webster, Florian Kobierska and Jan Magnusson of the SLF Snow Hydrology Group. We would also like to thank Dr. Nick Rutter from Northumbria University in Newcastle, UK for use of his working group's radiometer array.

References

Alexander, C., Moeslund, J.E., Bøcher, P.K., Arge, L., Svenning, J.C., 2013. Airborne laser scanner (LiDAR) proxies for understory light conditions. Remote Sens. Environ. 134, 152–161.

Breda, N., 2003. Ground-based measurements of leaf area index: a review of methods, instruments and current controversies. J. Exp. Bot. 54, 2403–2417.

Chang, M., 2003. Forest Hydrology: An Introduction to Water and Forests. CRC Press, Boca Raton, FL.

Essery, R., Bunting, P., Hardy, J., Link, T., Marks, D., Melloh, R., Pomeroy, J., Rowlands, A., Rutter, N., 2008. Radiative transfer modeling of a coniferous canopy characterized by airborne remote sensing. J. Hydrometeorol. 9, 228–241.

Fiala, A.C.S., Garman, S.L., Gray, A.N., 2006. Comparison of five canopy cover estimation techniques in the western Oregon Cascades. Forest Ecol. Manag. 232, 188–197.

Fleck, S.R.S., Cater, M., Schleppi, P., Ukonmaanaho, L., Greve, M., Hertel, C., Weis, W., Rumpf, S., 2012. Manual on methods and criteria for harmonized sampling, assessment, monitoring and analysis of the effects of air pollution on forests: Part XVII, leaf area measurements. In: United Nations Economic Commission for Europe International Co-operative programme on Assessment and Monitoring of Air Pollution Effects on Forests. ICP Forests, Hamburg.

Guntner, A., Stuck, J., Werth, S., Doll, P., Verzano, K., Merz, B., 2007. A global analysis of temporal and spatial variations in continental water storage. Water Resour. Res. 43 (5).

Hellström, R., 2000. Forest cover algorithms for estimating meteorological forcing in a numerical snow model. Hydrol. Processes 14, 3239–3256.

Huld, T., Šúri, M., Dunlop, E.D., 2008. Comparison of potential solar electricity output from fixed-inclined and two-axis tracking photovoltaic modules in Europe. Prog. Photovoltaics Res. Appl. 16, 47–59.

Hyer, E.J., Goetz, S.J., 2004. Comparison and sensitivity analysis of instruments and radiometric methods for LAI estimation: assessments from a boreal forest site. Agric. For. Meteorol. 122, 157–174.

Jonas, T., Essery, R., 2011. Snow cover and snowmelt in forest regions. In: Singh, V.P., Haritashya, U.K. (Eds.), Encyclopedia of Snow, Ice and Glaciers. Series: Encyclopedia of Earth Sciences Series. Springer, Dordrecht, Heidelberg, pp. 1033–1036.

Link, T.E., Marks, D., Hardy, J.P., 2004. A deterministic method to characterize canopy radiative transfer properties. Hydrol. Processes 18, 3583–3594.

Lovell, J.L., Jupp, D.L.B., Culvenor, D.S., Coops, N.C., 2003. Using airborne and ground-based ranging lidar to measure canopy structure in Australian forests. Can. J. Remote Sens. 29, 15.

Miller, J.B., 1967. A formula for average foliage density. Aust. J. Bot. 15 (1), 141–144.

Morsdorf, F., Kötz, B., Meier, E., Itten, K.I., Allgöwer, B., 2006. Estimation of LAI and fractional cover from small footprint airborne laser scanning data based on gap fraction. Remote Sens. Environ. 104 (1), 50–61.

Musselman, K.N., Margulis, S.A., Molotch, N.P., 2013. Estimation of solar direct beam transmittance of conifer canopies from airborne LiDAR. Remote Sens. Environ. 136, 402–415.

Musselman, K.N., Molotch, N.P., Margulis, S.A., Kirchner, P.B., Bales, R.C., 2012. Influence of canopy structure and direct beam solar irradiance on snowmelt rates in a mixed conifer forest. Agric. For. Meteorol. 161, 46–56.

Nobis, M., Hunziker, U., 2005. Automatic thresholding for hemispherical canopy-photographs based on edge detection. Agric. For. Meteorol. 128, 243–250.

Pomeroy, J., Ellis, C., Rowlands, A., Essery, R., Hardy, J., Link, T., Marks, D., Sicart, J.E., 2008. Spatial variability of shortwave irradiance for snowmelt in forests. J. Hydrometeorol. 9, 1482–1490.

Pomeroy, J.G., 1995. Snowcover: accumulation, relocation, and management. In: NHRI Science Report No.7. Springer, Saskatoon, Canada, http://www.ec.gc.ca/inre-nwri/default.asp?lang=En&n=0CD66675-1&offset=19&toc=show.

Riaño, D., Valladares, F., Condés, S., Chuvieco, E., 2004. Estimation of leaf area index and covered ground from airborne laser scanner (Lidar) in two contrasting forests. Agric. For. Meteorol. 124, 269–275.

Rosengrant, M., Cai, X., Cline, S., 2002. Global water outlook to 2025. In: A 2020 Vision for Food Agriculture and the Environment. International Food Policy Research Institute, Washington, DC, USA.

Rutter, N., Essery, R., Pomeroy, J., et al., 2009. Evaluation of forest snow processes models (SnowMIP2). J. Geophys. Res. D: Atmos. 114, 18.

Schleppi, P., Conedera, M., Sedivy, I., Thimonier, A., 2007. Correcting non-linearity and slope effects in the estimation of the leaf area index of forests from hemispherical photographs. Agric. For. Meteorol. 144, 236–242.

Schleppi, P., Paquette, A., 2014. Solar radiation in forests: theory for hemispherical photography. In: Fournier, R., Hall, R. (Eds.), Hemispherical Photography in Forest science: Theory, Methods, Applications. (in press).

Solberg, S., 2010. Mapping gap fraction, LAI and defoliation using various ALS penetration variables. Int. J. Remote Sens. 31, 1227–1244.

Solberg, S., Brunner, A., Hanssen, K.H., Lange, H., Næsset, E., Rautiainen, M., Stenberg, P., 2009. Mapping LAI in a Norway spruce forest using airborne laser scanning. Remote Sens. Environ. 113 (11), 2317–2327.

Stähli, M., Jonas, T., Gustafsson, D., 2009. The role of snow interception in winter-time radiation processes of a coniferous sub-alpine forest. Hydrol. Processes 23, 2498–2512.

Sturm, M., Holmgren, J., Liston, G.E., 1995. A seasonal snow cover classification system for local to global applications. J. Clim. 8, 1261–1283.

Thimonier, A., Sedivy, I., Schleppi, P., 2010. Estimating leaf area index in different types of mature forest stands in Switzerland: a comparison of methods. Eur. J. For. Res. 129, 543–562.

Timofeev, Y.M., Vasil'ev, A., 2008. Theoretical Fundamentals of Atmospheric Optics. Cambridge International Science Publishing, Cambridge, UK.

Varhola, A., Coops, N.C., 2013. Estimation of watershed-level distributed forest structure metrics relevant to hydrologic modeling using LiDAR and Landsat. J. Hydrol. 487, 70–86.

Varhola, A., Frazer, G.W., Teti, P., Coops, N.C., 2012. Estimation of forest structure metrics relevant to hydrologic modelling using coordinate transformation of airborne laser scanning data. Hydrol. Earth Syst. Sci. 16, 3749–4376.